Capillary Flow in Containers of Polygonal Section: Theory and Experiment

Mark M. Weislogel
TDA Research Inc., Wheat Ridge, Colorado

Since its founding, NASA has been dedicated to the advancement of aeronautics and space science. The NASA Scientific and Technical Information (STI) Program Office plays a key part in helping NASA maintain this important role.

The NASA STI Program Office is operated by Langley Research Center, the Lead Center for NASA's scientific and technical information. The NASA STI Program Office provides access to the NASA STI Database, the largest collection of aeronautical and space science STI in the world. The Program Office is also NASA's institutional mechanism for disseminating the results of its research and development activities. These results are published by NASA in the NASA STI Report Series, which includes the following report types:

- TECHNICAL PUBLICATION. Reports of completed research or a major significant phase of research that present the results of NASA programs and include extensive data or theoretical analysis. Includes compilations of significant scientific and technical data and information deemed to be of continuing reference value. NASA's counterpart of peer-reviewed formal professional papers but has less stringent limitations on manuscript length and extent of graphic presentations.

- TECHNICAL MEMORANDUM. Scientific and technical findings that are preliminary or of specialized interest, e.g., quick release reports, working papers, and bibliographies that contain minimal annotation. Does not contain extensive analysis.

- CONTRACTOR REPORT. Scientific and technical findings by NASA-sponsored contractors and grantees.

- CONFERENCE PUBLICATION. Collected papers from scientific and technical conferences, symposia, seminars, or other meetings sponsored or cosponsored by NASA.

- SPECIAL PUBLICATION. Scientific, technical, or historical information from NASA programs, projects, and missions, often concerned with subjects having substantial public interest.

- TECHNICAL TRANSLATION. English-language translations of foreign scientific and technical material pertinent to NASA's mission.

Specialized services that complement the STI Program Office's diverse offerings include creating custom thesauri, building customized data bases, organizing and publishing research results . . . even providing videos.

For more information about the NASA STI Program Office, see the following:

- Access the NASA STI Program Home Page at *http://www.sti.nasa.gov*

- E-mail your question via the Internet to help@sti.nasa.gov

- Fax your question to the NASA Access Help Desk at 301–621–0134

- Telephone the NASA Access Help Desk at 301–621–0390

- Write to:
  NASA Access Help Desk
  NASA Center for AeroSpace Information
  7121 Standard Drive
  Hanover, MD 21076

Capillary Flow in Containers of Polygonal Section: Theory and Experiment

Mark M. Weislogel
TDA Research Inc., Wheat Ridge, Colorado

National Aeronautics and
Space Administration

Glenn Research Center

Acknowledgments

Capillary Flow in Containers
of Polygonal Section: Theory and Experiment

Mark M. Weislogel
TDA Research Inc.
Wheat Ridge, Colorado 80033-1917

Abstract

An improved understanding of the large-length-scale capillary flows arising in a low-gravity environment is critical to that engineering community concerned with the design and analysis of spacecraft fluids management systems. Because a significant portion of liquid behavior in spacecraft is capillary dominated it is natural to consider designs that best exploit the spontaneous character of such flows. In the present work, a recently verified asymptotic analysis is extended to approximate spontaneous capillary flows in a large class of cylindrical containers of irregular polygonal section experiencing a step reduction in gravitational acceleration. Drop tower tests are conducted using partially-filled irregular triangular containers for comparison with the theoretical predictions. The degree to which the experimental data agree with the theory is a testament to the robustness of the basic analytical assumption of predominantly parallel flow. As a result, the closed form analytical expressions presented serve as simple, accurate tools for predicting bulk flow characteristics essential to practical low-g system design and analysis. Equations for predicting corner wetting rates, total container flow rates, and transient surfaces shapes are provided that are relevant also to terrestrial applications such as capillary flow in porous media.

Introduction

A significant portion of liquid behavior in spacecraft is capillary dominated: as for liquid propellants, cryogens, thermal fluids, and wastes. It is therefore natural to consider designs that best exploit the spontaneous character of such capillary surfaces and flows. Fundamental insights relevant to a variety of "characteristic" capillary flows continue to be sought that will further enable rapid and accurate predictions of important features of the fluid behavior.

Recent investigations have successfully demonstrated asymptotic techniques for the solution of capillary flows in containers with interior corners (see Ref. 1 and references contained therein). Such flows are "characteristic" of low-g fluid behavior in propellant tanks employing vanes or baffles for passive fluid positioning. In several cases, key features of the flow such as volumetric flow rate and surface shape may be determined in closed form—valuable tools to the designer of space-based fluids management systems.

The problem of sudden capillary rise (imbibition) in containers with interior corners is common to drop tower tests and serves as a model problem for liquid/tank filling, draining, response to thruster firing, docking, etc. In this paper an asymptotic analysis is briefly reviewed that has been successfully demonstrated to predict such flows in simple cylinders of rectangular and equilateral triangular section. The analysis is then generalized and extended to approximate flows in

cylindrical containers of irregular polygonal section with special attention paid to the development of a global similarity solution. Fully transient 3-D surfaces derived from the closed form expressions are presented for comparison with experiments. The results of simple drop tower tests employing irregular triangular containers are reported and the theoretical predictions are used to benchmark the salient features of the flow such as time dependent liquid column length and flow rate. Lastly, the value of the design relationships is briefly summarized.

Review of Ref. 1: Single Corner Solution

Detailed comparisons between experiments and theory have demonstrated the validity of the assumption that the flow throughout the container is controlled by the local capillary flow in the corner[1]. Assuming a wetting fluid and locally parallel flow [$(H/L)^2 \ll 1$], the dimensionless leading order governing equations simplify to the nonlinear lubrication PDE

$$h_\tau = 2h_z^2 + hh_{zz} \qquad (1)$$

where $h(z,\tau)$ is the dimensionless height of the meniscus measured along the bisector of the corner at location z and scaled time τ (see Figure 1 for notation). This governing equation implies that the surface may be approximated as a construct of circular arcs in the cross-flow plane (x-y plane), and, once $h(z,\tau)$ is determined, the entire 3-D transient surface may be determined from

$$S(y,h) = h(1+f) - (f^2h^2 - y^2\tan^2\alpha)^{1/2} \qquad (2)$$

The parameter f is the measure of interface curvature (driving force) and is given by

$$f = \left(\frac{\cos\theta}{\sin\alpha} - 1\right)^{-1}$$

where θ and α are the contact angle and corner half angle, respectively. The static contact angle boundary condition is correct to leading order and is thus applied at the contact line. Dynamic contact angle effects can be relegated to higher order, as the predominant flow direction is *parallel* to the contact line. Eq. (1) is in a general class of PDEs that emerge in nonlinear heat conduction[2] and foam drainage[3]. The problem of sudden capillary rise (imbibition) applies constraints $h(0,\tau) = 1$, $h(1,\tau) = 0$, and conservation of mass to Eq. (1). Transforming Eq. (1) by $h = F(\eta)$ and $\eta = z(2\tau)^{-1/2}$ yields the similarity equation

$$F F_{\eta\eta} + 2F_\eta^2 + \eta F_\eta = 0 \qquad (3)$$

subject to $F(\eta_{tip}) = 0$ and $F_\eta(\eta_{tip}) = -1/2$. Eq. (3) is invariant under the transformation $F = \lambda^2 F^+$ and $\eta = \lambda \eta^+$, which may be exploited so that the meniscus tip may be conveniently located at $\eta^+ = 1$, simplifying numerical calculation and producing the system

$$F^+ F^+_{\eta^+\eta^+} + 2F^{+^2}_{\eta^+} + \eta^+ F^+_{\eta^+} = 0 \qquad (4)$$

subject to $F^+(1) = 0$ and $F^+_\eta(1) = -1/2$. The numerical solution of $F^+(\eta^+)$ is provided in Figure 2. Because h is scaled by H, which is known, $\lambda^2 = [F(0)]^{-1/2}$, and with $F^+(0) \cong 0.345$, $\lambda \cong 1.702$. As mentioned above, the arbitrary and *dimensional* length L scales z, and the dimensionless time τ is given by

$$\tau = \frac{H}{2L^2} \frac{\sigma}{\mu} \frac{F_i \sin^2\alpha}{f} t \qquad (5)$$

where t is *dimensional* time, σ and μ are the fluid surface tension and dynamic viscosity, respectively, and $\sin^2\alpha / f$ is the geometric ratio of capillary driving force ($1/f$) to viscous resistance ($1/F_i \sin^2\alpha$). F_i is a weak function of θ and α (see Ref. 1, Fig. 6 for exact value).

The solution of Eq. (4) for a single interior corner of infinite length provides important design quantities such as liquid column length L and flow rate $\dot{Q}$ as functions of time. These quantities are provided below in *dimensional* form:

$$L = 1.702\, G^{1/2} H^{1/2} t^{1/2} \tag{6}$$

$$\dot{Q} = 0.349\, f^2 F_{An}\, G^{1/2} H^{5/2} t^{-1/2} \tag{7}$$

with

$$F_{An} = \frac{\cos\theta\cos(\alpha+\theta)}{\sin\alpha} - \frac{\pi}{2} + \alpha + \theta \tag{8}$$

and where H is a known constant height condition at $z = 0$. G is given by

$$G = \frac{\sigma F_i \sin^2\alpha}{\mu f} \tag{9}$$

With eqs. (6) through (9) low gravity containers may be sized, optimized, fluids selected, or flow times predicted. Such quantities, which can be rapidly computed with a calculator, are accurate to ±6% for perfectly wetting fluids[1] and represent an improvement over previous design relationships that used corner friction factors and weighted capillary pressures[4]. Even the flow in the vicinity of the bulk receding meniscus may be determined. Despite the fact that in this region the fundamental assumptions of parallel flow and 1-D interface curvature no longer apply, knowledge of the fluid removal rate from the bulk, which is well-described by the individual corner flows, enables the prediction of the bulk meniscus recede rate. The general concept behind the "global flow" solution was introduced in Ref. 1 and reveals similarly that the bulk meniscus axial location (for cylinders of regular polygonal section) obeys the relation

$$Z \propto \left(\sigma t/\mu\right)^{1/2} \tag{10}$$

the constant of proportionality being a function of specific container size and shape.

<u>Extension to *n*-Sided Polygonal Containers</u>

<u>General and Global Flow Characteristics</u>

The accuracy of the closed form expressions of eqs. (6), (7), and (10) have been established experimentally in drop tower tests employing equilateral triangular cylinders and rectangular cylinders of various aspect ratio[1] with $\theta = 0$. With this success, the solution approach may be generalized and extended to a large class of irregular polygons *without* re-entrant corners provided the Concus-Finn condition[1,5], $\theta < \pi/2 - \alpha_j$, is satisfied. A generalized irregular polygonal cylindrical section is shown in Figure 3 (left) to provide the necessary notation for the results to follow. The solution is limited to containers where the liquid "rises" independently in each corner that satisfies the Concus-Finn condition. The solution does not apply to irregular polygons where a single interface may span two or more corners. An example of such a container is depicted in Figure 3 (right) which may be only approximately analyzed using the techniques presented herein.

Employing the method of de Lazzer et al.[6] to evaluate the capillary pressure in the infinite container it is possible to show that

$$L_j = 1.702\, G_j^{1/2} H_j^{1/2} t^{1/2} \tag{11}$$

$$\dot{Q}_j = 0.349\, f_j^2 F_{An_j}\, G_j^{1/2} H_j^{5/2} t^{-1/2} \tag{12}$$

$$\dot{Q}_{tot} = \sum_{j=1}^{n} \dot{Q}_j$$

where

$$G_j = \frac{\sigma F_{ij} \sin^2 \alpha_j}{\mu f_j}, \quad f_j = \left(\frac{\cos \theta}{\sin \alpha_j} - 1 \right)^{-1}$$

$$H_j = \frac{R}{f_j} = \frac{P_n \cos \theta}{2 f_j \Sigma} \left[1 - \left(1 - \frac{4 A_n \Sigma}{P_n^2 \cos^2 \theta} \right)^{1/2} \right] \tag{13}$$

$$\Sigma = \sum_{j=1}^{n} F_{An_j}$$

$$F_{An_j} \equiv \frac{F_{Aj}}{f_j^2} = \frac{\cos \theta \cos(\alpha_j + \theta)}{\sin \alpha_j} - \frac{\pi}{2} + \alpha_j + \theta$$

where j denotes the jth of n interior corners. P_n and A_n are the perimeter and cross-sectional area of the n-sided polygon, respectively. It is useful to note from eqs. (11) and (12), that for a given polygonal vessel and fluid,

$$L_j \propto 1 - \sin \alpha_j \tag{14}$$

$$\dot{Q}_j \propto (1 - \sin \alpha_j)(\cot \alpha_j - \pi/2 + \alpha_j) \tag{15}$$

To give an example of the utility of these expressions, for a 45–45–90 isosceles triangular section the ratio

$$\frac{L_{45}}{L_{90}} \cong \frac{1 - \sin 22.5°}{1 - \sin 45°} = 2.10 \tag{16}$$

Therefore the liquid column in the 45° ($\alpha = 22.5°$)interior corner is always about 2.1 times longer than the liquid column in the 90° corner. A similar comparison may be made for $\dot{Q}_j$. The purely geometric relationships in eqs. (14) and (15) may be used to simplify hand calculations; the calculation of L_j and $\dot{Q}_j$ is necessary in only one corner, the Eq. (14) and (15) relationships are then used to form ratios by which to quickly determine L_j and $\dot{Q}_j$ in the remaining corners.

The results of eqs. (11) and (12) above are correct provided the coordinate origins for the individual corners are known. These are the locations of the constant pressure, constant height location (as determined by de Lazzer et al.[6]) boundary condition for the individual corners. Assuming that the coordinate origins for each corner coincide, a global similarity solution for the flow throughout the container is possible that is also fortunately consistent with the initial condition of a typical drop tower test. The pertinent details of this analysis are provided below. Further discussion of the "common origin" assumption is provided in a subsequent section.

In Figure 4 is sketched an irregular container section (left) with contrived interfaces shown in profile along the B-B plane of symmetry (right). The corner rise rates are different in corners of different α, and the assumed common origin is identified where the constant height condition $h_j(0, \tau) = 1$ for each corner applies. Because the details of the corner flows are known precisely in the domain $0 < z_j < (z_{tip})_j$, the objective of this "global" analysis is to provide the interface shapes within $z_b < z < 0$ and compute the bulk meniscus location z_b as well. The assumption of parallel flow in the individual corners is valid throughout the domain, $z_b < z_j < (z_{tip})_j$: note that $(z_{tip})_k = L_k$.

The analysis begins with a *dimensional* mass balance about the origin, noting that the volume of fluid drawn up the corners ($z > 0$) is equal to the volume of fluid removed from the bulk ($z < 0$); the volumes of the cross-hatched regions above and below $z = 0$ in Figure 4 are equal. Therefore, noting $z_b < 0$,

$$\sum_{j=1}^{n} \int_{0}^{z_{tipj}} F_{Aj}\, h_j^2\, dz = -A_n\, z_b - \sum_{j=1}^{n} \int_{z_b}^{0} F_{Aj}\, h_j^2\, dz$$

where $F_{Aj} = f_j^2 F_{Anj}$. Combining terms yields

$$A_n\, z_b + \sum_{j=1}^{n} \int_{z_b}^{z_{tipj}} F_{Aj}\, h_j^2\, dz = 0 \tag{17}$$

Nondimensionalizing h_j and z by H_j and L, and introducing similarity functions $h_j = F_j(\eta_j)$, $\eta_j = z(2\tau_j)^{-1/2}$, $\eta_{tipj} = z_{tipj}(2\tau_j)^{-1/2}$, and $z_b = \eta_{br}(2\tau_r)^{1/2}$, as accomplished for the governing similarity ODE Eq. (3), Eq. (17) is transformed to

$$A_n + \sum_{j=1}^{n} \frac{F_{Aj} H_j^2}{\eta_{br}} \left(\frac{\tau_j}{\tau_r}\right)^{1/2} \int_{\eta_{br}(\tau_r/\tau_j)^{1/2}}^{\eta_{tipj}} F_j^2\, d\eta_j = 0 \tag{18}$$

The global similarity solution naturally assumes that the bulk meniscus location behaves according to the $t^{1/2}$ law and employs a reference time scale based on arbitrary reference angle α_r, interface height H_r, and interface curvatures f_r reminiscent of Eq. (5), namely

$$\tau_r = \frac{H_r}{2L^2} \frac{\sigma}{\mu} \frac{F_{ir} \sin^2 \alpha_r}{f_r} t$$

Thus, noting $H_j = R/f_j$ from Eq. (13),

$$\left(\frac{\tau_r}{\tau_j}\right)^{1/2} = \frac{f_j \sin \alpha_r}{f_r \sin \alpha_j} \left(\frac{F_{ir}}{F_{ij}}\right)^{1/2}$$

Note that the weak functional dependence of F_{ij} is considered despite the fact that this parameter is bound $1/8 < F_{ij} \le 1/6$ for all possible values of θ and α_j. Substituting invariant transform functions $\eta_j = \lambda_j\, \eta_j^+$ and $F_j = \lambda_j^2\, F_j^+$, Eq. (18) transforms to

$$A_n + \sum_{j=1}^{n} \frac{\lambda_j^5}{\lambda_r} \frac{F_{Aj} H_j^2}{\overline{\eta}_{br}^+ B_j} \int_{\overline{\eta}_{br}^+ B_j}^{1} F_j^{+2}\, d\eta_j^+ = 0 \tag{19}$$

where

$$\overline{\eta}_{br}^+ \equiv \frac{\eta_{br}^+ F_{ir}^{1/2} \sin \alpha_r}{f_r}$$

and

$$B_j \equiv \frac{f_j}{F_{ij}^{1/2} \sin \alpha_j}$$

At this point it is clear from Eq. (19) that the integrand is independent of corner j, thus $\lambda_j = \lambda_r = \lambda$ and, after further rearrangement noting $H_j = R/f_j$ and $F_{Aj} = f_j^2\, F_{Anj}$, Eq. (19) simplifies to

$$\frac{\overline{\eta}_{br}^+ A_n}{R^2} + \sum_{j=1}^{n} \frac{F_{Anj}}{B_j} \int_{\overline{\eta}_{br}^+ B_j}^{1} (\lambda^2 F^+)^2\, d\eta^+ = 0 \tag{20}$$

which must be solved implicitly for $\overline{\eta}_{br}^+$ once F^+ is computed from the invariant similarity ODE, Eq. (4). As previously stated, the solution for F^+ shown in Figure 2 gives $F^+(0) = 0.345...$ which yields $\lambda = 1.702...$ It may also be shown that as η^+ becomes increasingly negative, $F^+(\eta^+)$ asymptotically approaches $-0.465...$ Thus, from Eq. (20) it may be shown that as $\cos\theta - \sin\alpha_j$ approaches 0 for a given corner the volumetric flow along the corner contributes negligibly to the value of $\overline{\eta}_{br}^+$.

Computed values for $\overline{\eta}_{br}^+$ from Eq. (20) are listed in Table 1 for a variety of familiar container cross sections. In the limit $|\overline{\eta}_{br}^+ B_j| \ll 1$ it may be shown that

$$\overline{\eta}_{br}^+ \approx \frac{-0.4103 \sum\limits_{j=1}^{n} F_{Anj} F_{ij}^{1/2} (\cos\theta - \sin\alpha_j)}{\dfrac{A_n}{R^2} - \sum\limits_{j=1}^{n} F_{Anj}} \tag{21}$$

which is a leading order expression revealing most clearly the general dependence of $\overline{\eta}_{br}^+$ on the geometry of the system. Values of $\overline{\eta}_{br}^+$ computed from Eq. (21) are also listed in Table 1 where it is seen that errors incurred are < 2% for most of the containers listed. Errors using Eq. (21) increase significantly however for small corners α_j and slight curvature $\cos\theta - \sin\alpha_j$, where $|\overline{\eta}_{br}^+ B_j| \ll 1$ is no longer true.

With $\overline{\eta}_{br}^+$ known, the *dimensional* bulk meniscus location is found from

$$z_b = 1.702 \overline{\eta}_{br}^+ \left(\frac{R\sigma}{\mu} t\right)^{1/2} \equiv K_{zb} t^{1/2} \tag{22}$$

and because $\overline{\eta}_{br}^+ < 0$, z_b is of course increasingly negative in time. Cast in this form it is insightful to note that the liquid column length in each corner from Eq. (11) is

$$L_j = 1.702 F_{ij}^{1/2} (\cos\theta - \sin\alpha_j) \left(\frac{R\sigma}{\mu} t\right)^{1/2} \equiv K_{Lj} t^{1/2} \tag{23}$$

and the total active interface length for each corner may be determined by

$$L_{totj} = L_j - z_b = 1.702 \left(\frac{R\sigma}{\mu} t\right)^{1/2} \left(F_{ij}^{1/2}(\cos\theta - \sin\alpha_j) - \overline{\eta}_{br}^+\right) \equiv K_{totj} t^{1/2} \tag{24}$$

Thus, the global similarity solution is given by Eq. (23) for the corner flows, Eq. (22) for the receding bulk meniscus, and Eq. (24) for the total "hydrodynamically active length" along each corner.

Discussion on Global Solutions

Included in Table 1 is a term Q_{geom} that represents the geometric dependence of the total flow rate along the interior corners of the container,

$$Q_{geom} \equiv 100 R^{5/2} \sum\limits_{j=1}^{n} F_{Anj} F_{ij}^{1/2} (\cos\theta - \sin\alpha_j) \propto \dot{Q}_{tot} \tag{25}$$

Q_{geom} is computed for each cross-section holding cross-sectional area fixed. It is important to note that Q_{geom} and thus Q_{tot} tracks with $\bar{\eta}_{br}^+$. It is also important to note that Q_{geom} changes dramatically with container shape for fixed cross-sectional area. For example, the equilateral rhombic sections computed in Table 1 reveal at least a 23-fold increase in volumetric flow rate as the acute angle is reduced. These trends illustrate that for fixed cross-sectional area, containers with a larger number of smaller corner angles will transport significantly larger amounts of liquid by capillary forces, i.e. a porous material with 30-150 ($\equiv 30°$-$150°$) equilateral rhombic channels will transport 9-fold the liquid of a porous material with 90-90 equilateral rhombic channels with the same total cross sectional area! It can be shown that $Q_{tot} \propto \alpha^{1/4}$ and thus approaches zero slowly for vanishingly small values of α as indicated by reduced value of Q_{geom} listed in Table 1 for a 0.11-179.9 equilateral rhombus. Q_{geom} values for the regular n-gons approach zero with increasing n as expected.

Detailed Interfacial Results

Perhaps the most important design quantities summarizing such flows are provided above in eqs. (11), (12), and (22). However, the entire surface profile of the liquid throughout the container may be computed if desired. The solution follows from the generalized global similarity solution and is applicable at long times throughout the container, despite the fact that both the flow and interface shape are not known in the neighborhood of the bulk meniscus. By approximating the global similarity solution for the meniscus centerline height in each corner by the polynomial

$$h_j = H_j(1 - 0.571\eta^+ - 0.429\eta^{+^2})$$

(26)

where H_j is given by Eq. (13) and

$$\eta^+ = 0.587\left(\frac{\mu f_j}{\sigma H_j (F_i)_j \sin^2\alpha_j}\right)^{1/2} z t^{-1/2}$$

(27)

subject to the constraint $\bar{\eta}_{br}^+ B_j \leq \eta^+ \leq 1$, the 3-D transient interface in each corner may be computed via

$$S_j = h_j(1 + f_j) + (h_j^2 f_j^2 - y_j^2)^{1/2}$$

(28)

where

$$\left| y_j \right| \leq h_j f_j \cos(\alpha_j + \theta)$$

Samples of computed surfaces using this simple approach are presented in Figure 5 for 45-45-90 and 30-60-90 triangular cylinders. Note that the column length for the 45° corner is about 2.1 times that of the 90° corner as predicted by Eq. (16). These results extend previous solutions for equilateral polygons[7].

Impact of Approximations

Essential to the analyses above is the assumption that the constant height condition for each corner occurs at a common z-coordinate origin. The validity of this assumption has not been fully established, but it will be demonstrated experimentally that the general solution approach is rather insensitive to the precise location of the coordinate origin(s). The common origin assumption permits a global similarity solution that perhaps best captures the initial condition of typical drop tower tests. However, there are certainly unphysical characteristics of the solution at small times. In Figure 6 is shown 3 frames of a drop tower test the details of which will be provided in the experiments section. For the similarity solution the constant height location H_j for

the subject corner flow occurs at what is assumed to be the z-coordinate origin ($z = 0$) for each corner flow. It is important to note that this location does not coincide with the initial interface origin, nominally identified by z_o on the figure. The global similarity solution assumes that the volume of the gas phase above the interface and below the $z = 0$ dashed line at $t = 0$ is approximately if not precisely equal to the volume of vapor above the bulk meniscus and below the $z = z_b$ line at $t = 2.23$s. In this way the similarity solution is only concerned with the region $z_b < z < z_{tipj}$ where the assumptions of parallel flow and 1-D interface curvature apply. This argument serves also to explain the discontinuous nature of the bulk interface at z_b depicted in Figure 4.

For certain container cross-sections of extreme aspect ratio, no value for $\overline{\eta}_{br}^+$ may be computed. For example, the 6.5-173.5 equilateral rhombus in Table 1 is the last rhombic section that will permit a solution for $\overline{\eta}_{br}^+$ satisfying Eq. (20). In the limit of $\alpha_j \ll 1$ and $\cos\theta - \sin\alpha_j \ll 1$, $|\overline{\eta}_{br}^+ B_j|$ becomes increasingly large and z_b moves sufficiently upstream to the point where the interfaces in each corner join to form the inscribed circle to the container. At this point the global similarity solution is unable to compute z_b (though $L(t)$ and $Q(t)$ remain valid) and z_b and L are of equal order. This implies that the bulk meniscus recede rate is comparable to the tip rise rate. It is conjectured that such limiting vessels possess a region dominated by curvature associated with the inscribed circle with communication between corners, and where the interface may be influenced by the Rayleigh instability at long times. No experimental support to this claim is offered.

For the majority of possible containers, solution to the common origin problem provides the common value of z_b for all corners. Thus, it is possible to compute the *dimensional* capillary under-pressure at z_b in each corner, namely

$$P_j = -\frac{0.345\sigma}{RF^+(\overline{\eta}_{br}^+ B_j)} \tag{29}$$

where $\overline{\eta}_{br}^+ B_j$ is the lower limit of the integral in Eq. (20). Differences in P_j values at z_b between corners can provide some insight into the nature of the common origin solution. Obviously, the common origin assumption is correct for regular n-gons and rectangles since the flow in each corner is identical. Recalling that for sufficiently negative η^+, $F^+ = const.$, and P_j of Eq. (29) approaches a constant at z_b for all corners; a further validation of the common origin assumption for containers where $|\overline{\eta}_{br}^+ B_j| \gg 1$ is satisfied in each corner. An example of such a container is approached by the geometry of the 6.5-173.5 rhombus in Table 1. However, for other container cross-sections, the individual corner capillary under-pressures at z_b differ by as much as the theoretical maximum of 26%. If the common origin assumption is correct for these flows too, the differences in pressures at z_b between corners must be accommodated within the region of bulk meniscus curvature, which has been shrunk to a zero thickness region as sketched in Figure 4 and discussed above.

The analytical approach applies in general if the Concus-Finn condition $\theta < \pi/2 - \alpha_j$ is satisfied in at least one interior corner of the container. The special case of the Concus-Finn condition being met in all corners is presented above and supported by experiments performed herein. However, it is important to note that for systems exhibiting partial wetting, $\theta_j > 0$, contact angle hysteresis may result in significant departures from the above predictions. Also, the analysis at

present is limited to polygonal containers without re-entrant corners, though containers with re-entrant corners and smoothly curved portions may be treated with a similar approach.

Drop Tower Experiments

Simple experiments to corroborate the theoretical predictions are performed using the 2.2s drop tower at NASA's Glenn Research Center. Partially filled cylinders of triangular cross-section are secured to a drop frame, backlit by diffuse light source, and photographed at long working distance by a B/W digital video recorder. Release of the experiment package into free fall signals the onset of the spontaneous "capillary rise" (imbibition) along the interior corners of the container. Sample video images are provided in Figure 7 for a typical drop test, where the wetting liquid is observed to redistribute along the corners of the container with the step-reduction of gravity, see also Figure 6. The difference in wetting rates due to the different corner angles is obvious from such tests. The test fluids used are perfectly wetting liquids on acrylic, 2 and 5sc Si oil, and the relevant fluid properties are included in Table 2.

Test Cell and Test Description

Two test-case prismatic vessels are fabricated for the experiments: 30-60-90 and 45-45-90 right triangles. The vessels are fabricated using precision-machined acrylic sections that are carefully fused then annealed. To ensure accurate interface height measurements perpendicular to the corner axis with minimal though calculable corrections for optical distortion, the test vessels are constructed such that the plane bisecting the corner angle of concern is perpendicular to the camera line of sight. Figure 8 illustrates the cross-section of the cells tested and provides some dimensions.

Figure 8 also indicates the fused surfaces necessary for vessel fabrication. The 90° corners are milled using a zero radius tool. Two each of the vessels are fabricated, the nominal details of which are included in Table 2. Some of the experiments are performed at low magnification to determine liquid column length (tip length) as a function of time $L(t)$, i.e. Figure 7. Other tests at higher magnification are performed to determine the bulk meniscus location $Z(t)$ and transient surface elevations $h(z,t)$, i.e. Figure 6. Each test is repeated up to 7 times to verify repeatability as well as uniformity of test cell dimensions and corner quality. The Tracker Image Analysis System developed by NASA[8] is used to digitize the video images. Where possible an intensity threshold algorithm is employed to automatically identify and track the interface frame by frame. Measurement accuracy could be determined to be within ±0.38mm for the low magnification $L(t)$ tests and within ±0.12mm for the higher magnification $Z(t)$ and $h(z,t)$ tests.

Results and Discussion

Raw data for the corner tip location $L(t)$ and bulk meniscus location $Z(t)$ are plotted in Figure 9 for 5cs Si oil in the 30-60-90 right triangular vessel. The initial z-coordinate location of the bulk meniscus at $t = 0$, z_o (see Figure 6), is used as the reference for these measurements. Two tests each are provided on the plot to illustrate repeatability. The differences in tip location for the different corners of the vessel are plain to see and quantify.

In Figure 10 through Figure 15, $L(t)$ or $Z(t)$ is plotted against $t^{1/2}$ as suggested by theory. The linear nature of these figures is reassuring. In Figure 10 and Figure 11, $L(t)$ is presented as a function of corner angle for the 30-60-90 triangle for 2 and 5cs Si oil, respectively. In Figure 12 and Figure 13, $L(t)$ is presented as a function of corner angle for the 45-45-90 triangle for 2 and

5cs Si oil, respectively. In all four figures the theoretically determined rise rate K_{Lj} from Eq. (23) is superposed using a dashed line for comparison to the experiments. The level of agreement observed fortifies the functional dependence of the untested parameters captured by the analysis leading to eqs. (22) and (23); namely, container size, shape, and surface tension, in addition to the tested parameters of corner angle, fluid viscosity, and time.

Acceptable agreement is achieved in all cases, but appears to worsen in the double limit of increased corner angle and time. Experimental uncertainty is suspected for the observed "falling off" of the experimental data from the theoretical slope. For corner angles above 30°, as the corner angle increases, the amount of liquid rising in the corner rapidly decreases to the image resolution at the tip. Combined with increased optical distortion for the larger angles, the tip location measurement technique employed becomes increasingly difficult as the liquid column lengthens. This is not the case at short times where there is no ambiguity in tip location, which perhaps best explains the agreement of K_L with the data at short times for the larger corner angles. The fact that the 90° corners are machined rather than fused may also play a role retarding the flow as h becomes vanishingly small at the tip. The smaller the corner angle the more accurate the data and the better the agreement between K_L and the data over the entire test duration. Computed and experimentally determined values for K_L are listed for comparison in Table 4. Nominal values differ by less than ±6%.

In Figure 14 and Figure 15, $Z(t)$ is presented vs. $t^{1/2}$ for the 30-60-90 and 45-45-90 triangles for 2 and 5cs Si oil. Multiple data sets using shaded and unshaded symbols are presented to indicate repeatability. K_{zb} of Eq. (22) is superposed on the figures using dashed lines and in all cases is in favorable agreement with the data as listed in Table 3. Because $z_b(t) = Z(t)$ only for large t, $z_b(t)$ predicted by the global similarity analysis requires longer times before agreement with the data than the $L(t)$ predictions.

The level of agreement shown in Figure 10 through Figure 15 and Table 3 and 4 is a positive argument supporting the simplifying theoretical assumption of a common pressure (constant height) location for all corners which serves as the origin for all coordinate systems.

Further data along these lines is presented in Figure 16 and Figure 17 for the 45-45-90 triangle, 2cs fluid, where $h(z_i,t)$ is plotted for a variety axial locations z_i for both 45° and 90° corners, respectively. The z-coordinate location of $h(z_i,t)$ is referenced to the location of the bulk meniscus centerline z_o at $t = 0$. Points z_i above and below the true constant height location are selected for digitization. $h(z_i,t)$ values below the constant height location decrease in time to H_i while $h(z_i,t)$ values above the constant height location increase in time to H_i. The z-coordinate location of H_i may be determined by interpolation to empirically identify the $h(z_i,t)$ curve that most rapidly achieves a constant value in time.

Unfortunately, these data suffer increased uncertainty due to pixel resolution limits, especially in identifying the location of the corner axis. However, this difficulty introduces an offset to the family of curves without affecting the relative relationship of one $h(z_i,t)$ curve to another, though the slopes at large times are also somewhat difficult to compute. The theoretical constant height value computed from Eq. (13) is included as a dashed horizontal line in each figure and, in part, indicates the magnitude of the offset which appears small in Figure 16 and Figure 17.

Thus, it is possible to determine a range of possible values for the coordinate origin z_H for both 45° and 90° corners. For example, from Figure 16 it can be discerned that in general $3.50 < z_H < 4.56$mm for the 45° corner, whereas from Figure 17, $3.28 < z_H < 4.07$mm for the 90° corner. This at least implies that differences in Z_H values between corners, if any, are small $< O(1.3\text{mm})$ and certainly negligible compared to the overall liquid column length $> O(50\text{mm})$. This result also supports the use of the significantly simplifying assumption of a common z-coordinate origin for each of the corner flows.

Concluding Remarks

The results of an analysis predicting low-g capillary flows in containers with interior corners is presented that is based on parallel flow along any interior corner of the container satisfying the Concus-Finn wetting condition. The results apply to a large class of cylindrical containers with at least one interior corner where the global capillary curvature may be computed via the technique of de Lazzer et al.[6], i.e. cylinders of polygonal section that are devoid of re-entrant corners. The strength of the global solution is that the complexities of solving both for the flow and interface shape in the region of the bulk interface are avoided due to the highly accurate corner flow solutions that control the liquid removal rate from the bulk.

Closed form expressions are presented to predict important features of the flow such as liquid column length in each corner Eq. (23), corner and/or total container flow rate Eq. (12), and meniscus recede rate Eq. (22). Fully transient 3-D interfaces may also be quickly computed, see eqs. (26)-(28) and Figure 5. Drop tower experiments conducted to verify the theoretical predictions vary interior corner angle and fluid viscosity in 30-60-90 and 45-45-90 right triangular cylindrical containers. The nominally ±6% agreement between the simple hand- or spreadsheet-calculated quantities and the experimental data suggests that the untested functional dependence of container size, shape, and surface tension are also correctly captured by the analysis, see Table 3 and 4.

The assumption of a common coordinate origin for each corner flow enables the global similarity solution. Comparison with experiments reveals that the resulting flows are rather insensitive to this assumption. The closed form expressions derived and benchmarked herein are suitable tools for efficient low-g fluids system design such as for the prediction of tank filling characteristics, the reorientation and settling transients in vaned containers, and the distribution of flows within containers with a variety of interior corners. The results are also applicable to terrestrial applications where the influence of gravity is small; i.e. porous wick structures in heat pipes, capillary pumped loops. Valuable insights concerning optimum container/pore design may be determined in part by inspection of the closed form results. For example, it is shown that a 30-150 equilateral rhombic section/pore is capable of 9-times the flow capacity of a square section of identical area.

References

[1]M.M. Weislogel, S. Lichter, "Capillary Flow in Interior Corners," *Journal of Fluid Mechanics*, Vol. 373, 1998, pp. 349-378.

[2]F.J. Mayer, J.F. McGrath, J.W. Steele, "A Class of Similarity Solutions for the Nonlinear Thermal Conduction Problem," *Journal of Physics A: Math. Gen.*, Vol. 16, 1983, pp. 3393-3400.

[3]G. Verbist, D. Weaire, A.M. Kraynik, "The Foam Drainage Equation, *Journal of Physics: Condensed Matter*, Vol. 8, 1996, pp. 3715-3731.

[4]D.E. Jaekle Jr., "Propellant Management Device Conceptual Design and Analysis: Vanes," AIAA-SAE-ASME-ASEE 27th Joint Propulsion Conference, AIAA-91-2172, Sacramento, CA, June 1991.

[5]P. Concus; R. Finn, "On the Behavior of a Capillary Surface in a Wedge," *Proceedings of the Academy of Sciences.,*Vol. 63, No. 2, 1969, pp. 292-299.

[6]A. de Lazzer, D. Langbein, M. Dreyer, J. Rath, "Mean Curvature of Liquid Surfaces in Containers of Arbitrary Cross-Section, *Microgravity Science and Technology,* Vol. IX, No. 3, 1996, pp. 208-219.

[7]M.M. Weislogel, "Fluid Interface Phenomena in a Low-Gravity Environment: Recent Results from Drop Tower Experimentation," *Space Forum Journal*, Vol. 3, 1998, pp. 59-86.

[8]R.B. Klimek, T.W. Wright, R.S. Sielken, "Color Image Processing and Object Tracking System," NASA Technical Memorandum 107144, NASA Glenn Research Center, 1996.
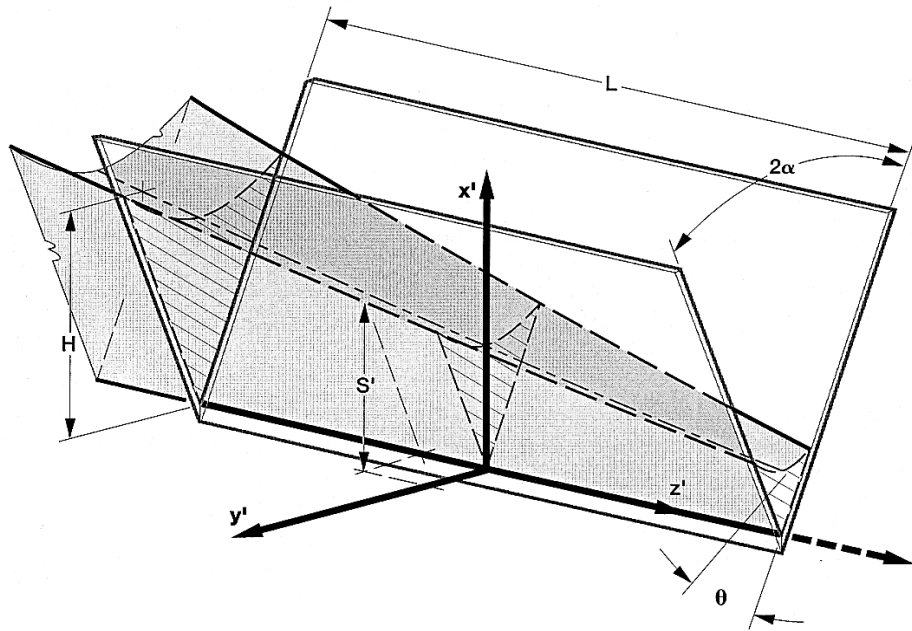
Figure 1. Fluid column in an isolated corner, angle 2α. The 3-D surface profile is $S(y,z,t)$ with characteristic height and length, H and L, respectively.
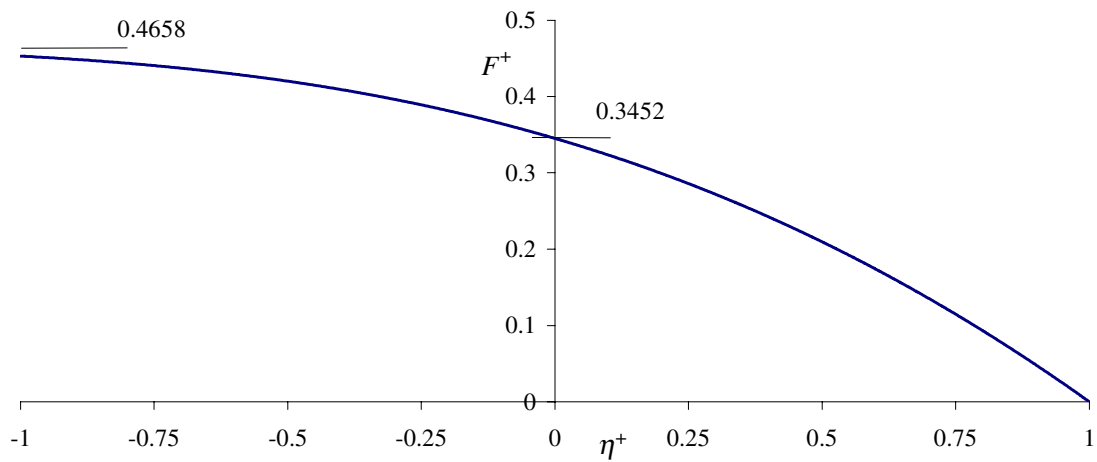
Figure 2. Invariant similarity solution for corner flow, Eq. (4).
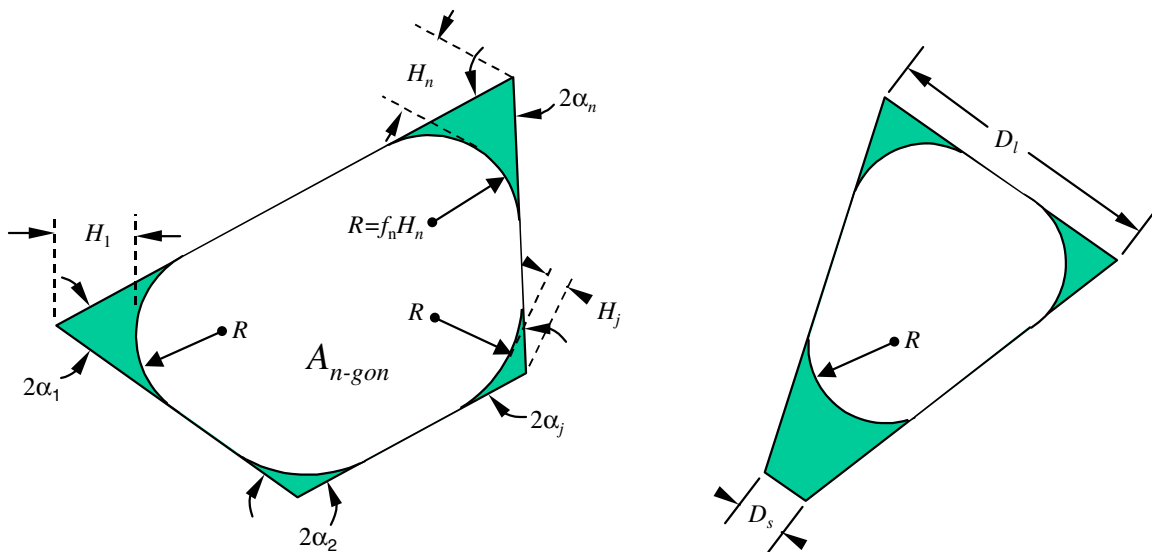
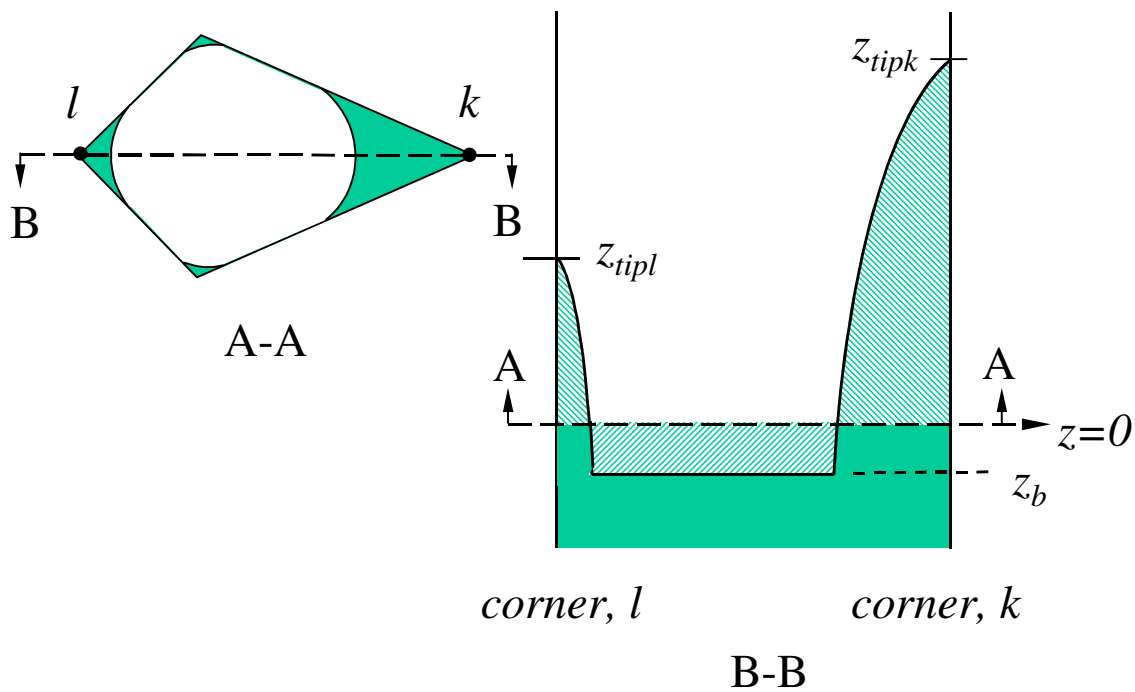Figure 3. Left, notation for *n*-sided polygon. Right, example *n*-gon not addressed herein.

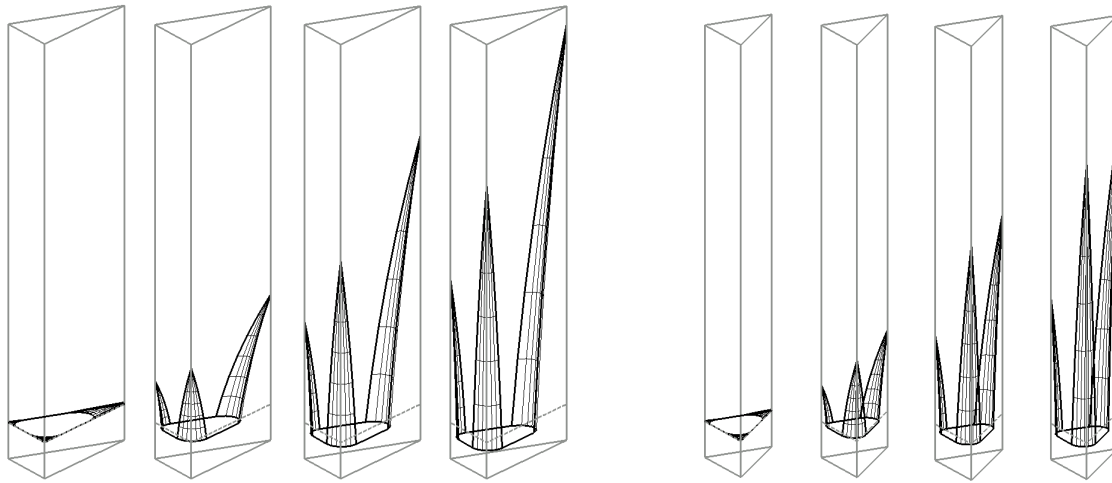Figure 4. Notation for global similarity solution in irregular *n*-gon.

Figure 5. Computed surfaces employing eqs. (26) through (28): Left, 30-60-90 and Right, 45-45-90 right triangles. Surfaces at time 0, 0.05, 0.3 and 0.6s are shown for 2cs Si Oil in containers listed in Table 1.
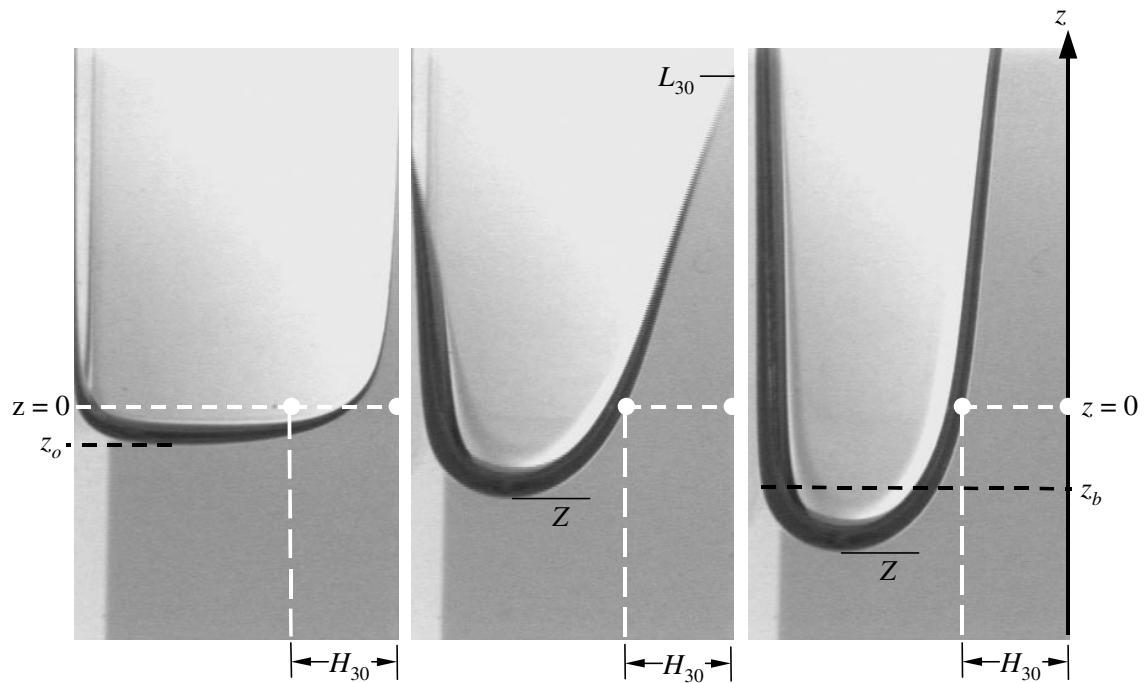
Figure 6. Capillary rise in 30° corner of 30-60-90 container, 5cs Si oil ($t = 0$, 0.37, 2.23s). Vessel is oriented as the vessel in the lower left corner of Figure 8. Notation identified for discussion of global similarity solution.
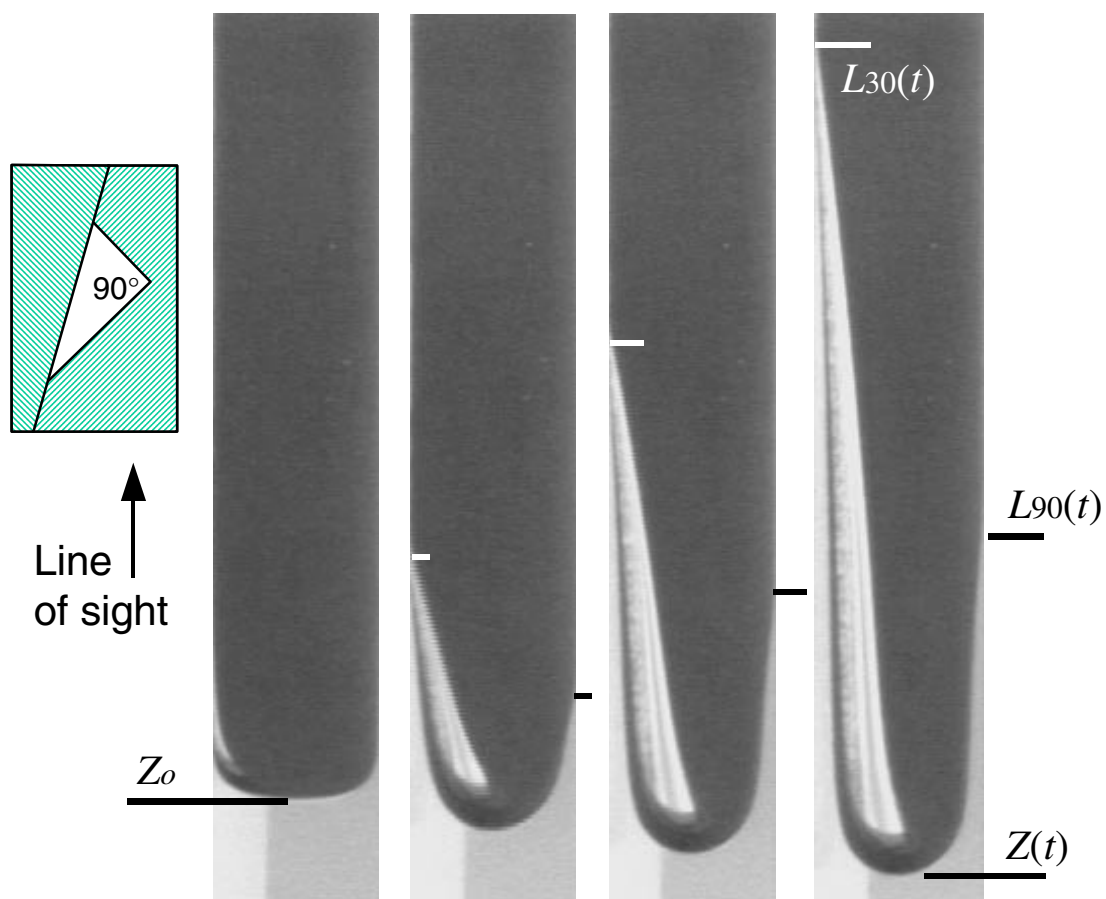
Figure 7. Drop tower test: capillary rise in 30-60-90 triangle at times 0, 0.23, 0.7 and 1.63s. Quantitative test for 90° corner, right side of image, 5cs Si oil.
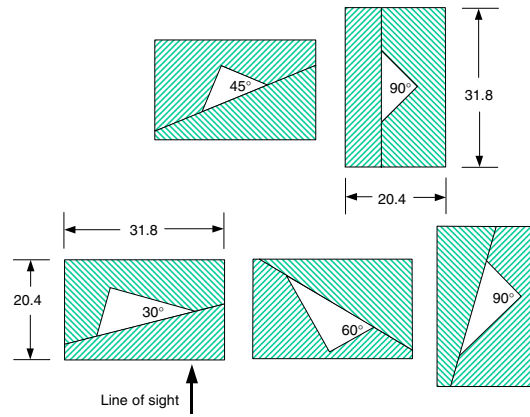
Figure 8. Test cell sections: quantitative test angle noted (dimensions in mm).
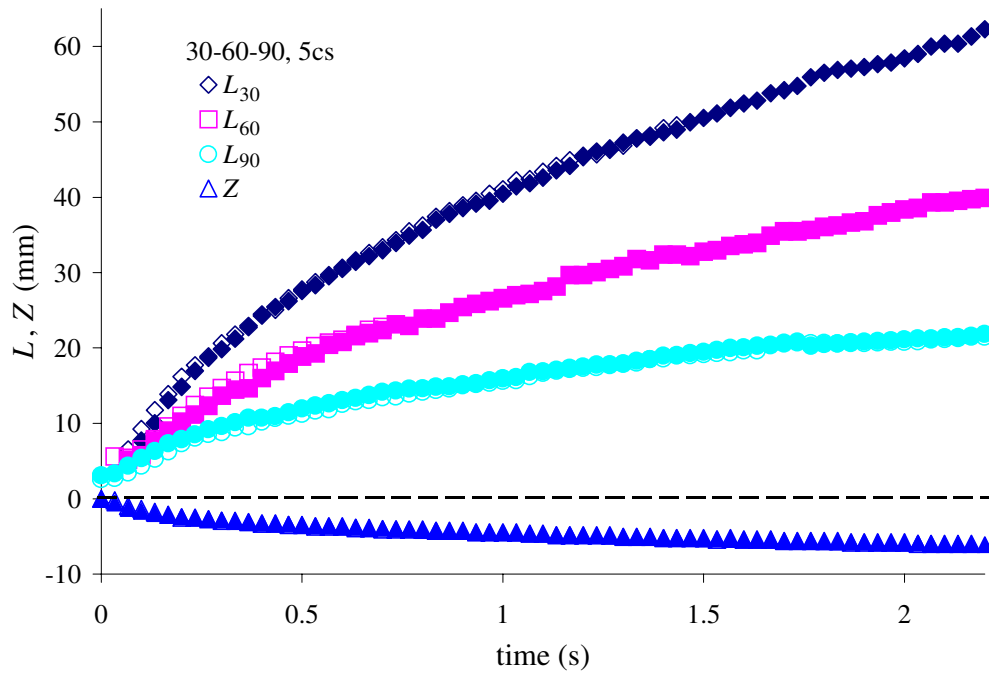
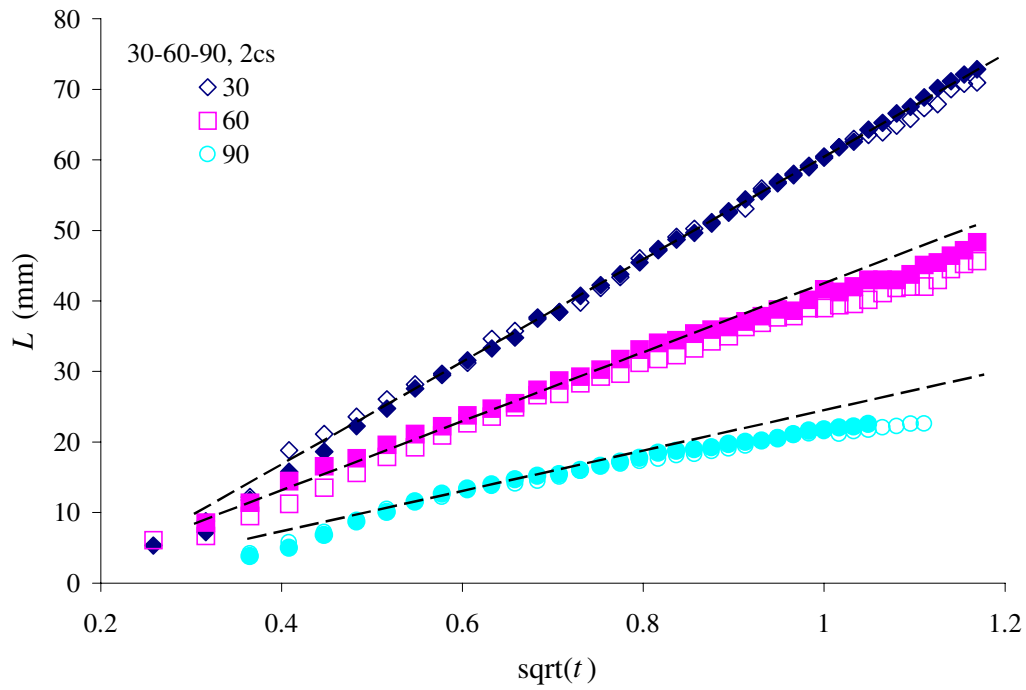Figure 9. Raw $L(t)$ and $Z(t)$ data, for 30-60-90 triangle, 5cs Si oil.

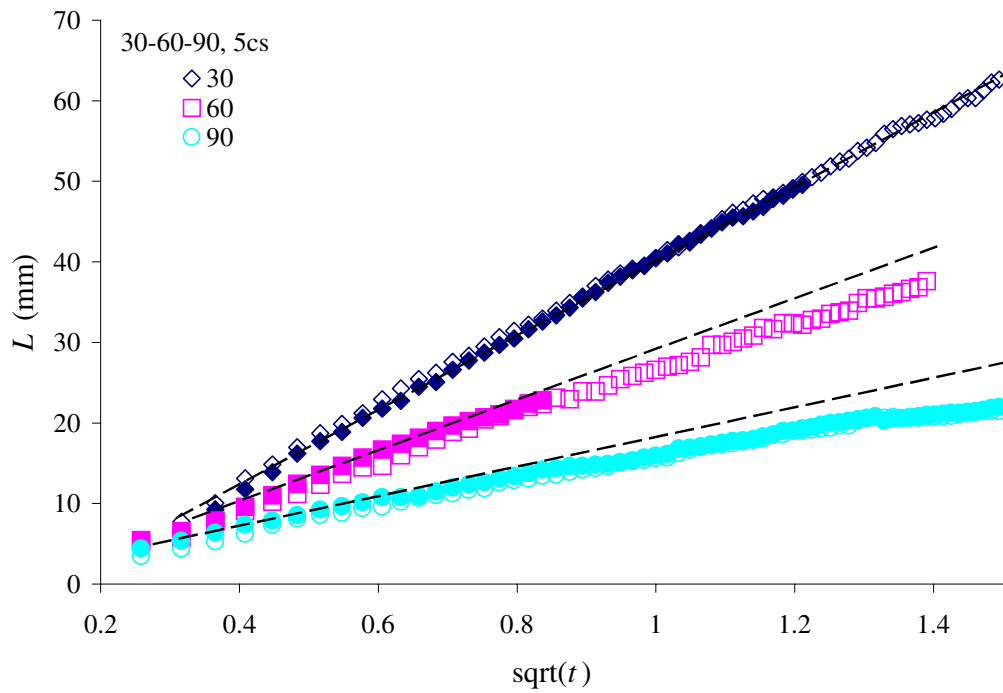Figure 10. *L*(*t*) vs. *t*^{1/2} in 30-60-90 with 2cs.

s

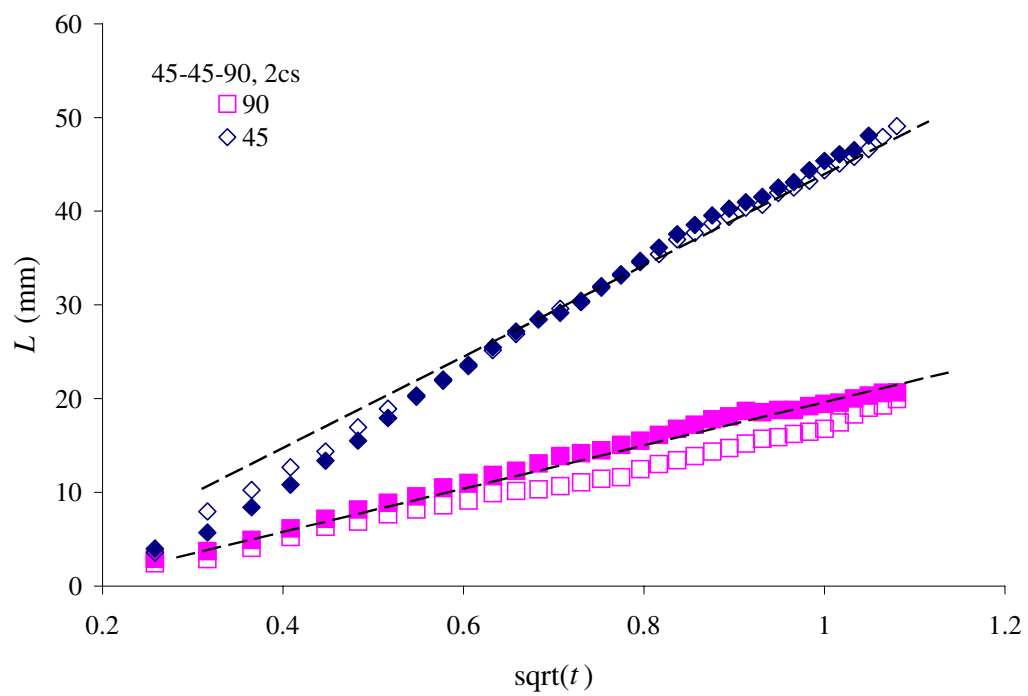
Figure 11. *L*(*t*) vs. *t*^{1/2} in 30-60-90 with 5cs.

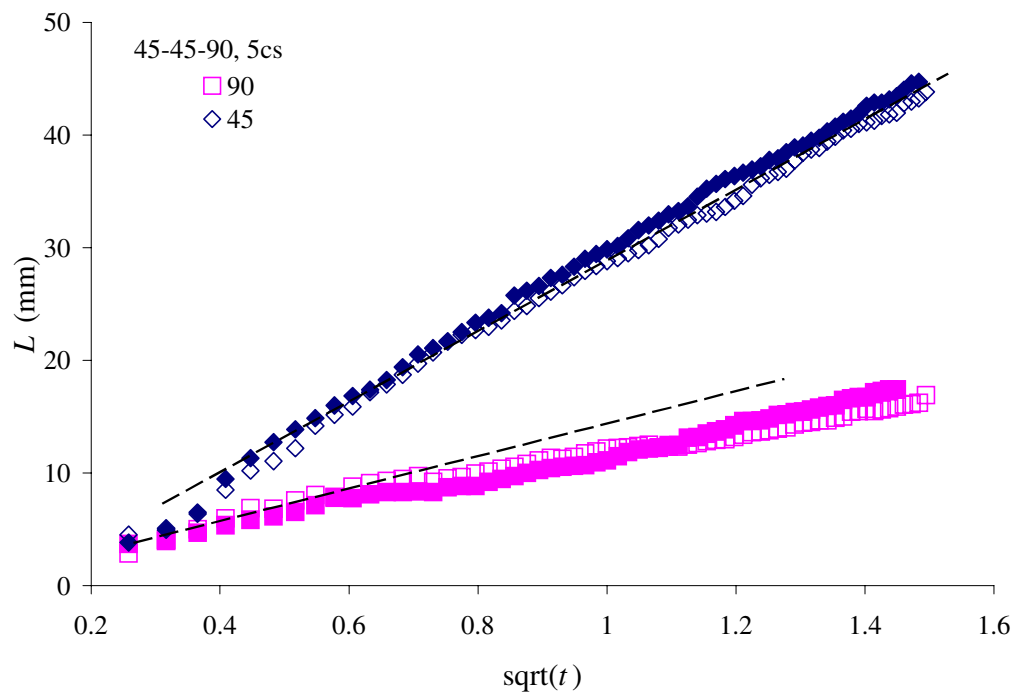Figure 12. $L(t)$ vs. $t^{1/2}$ for 45-45-90, 2cs.
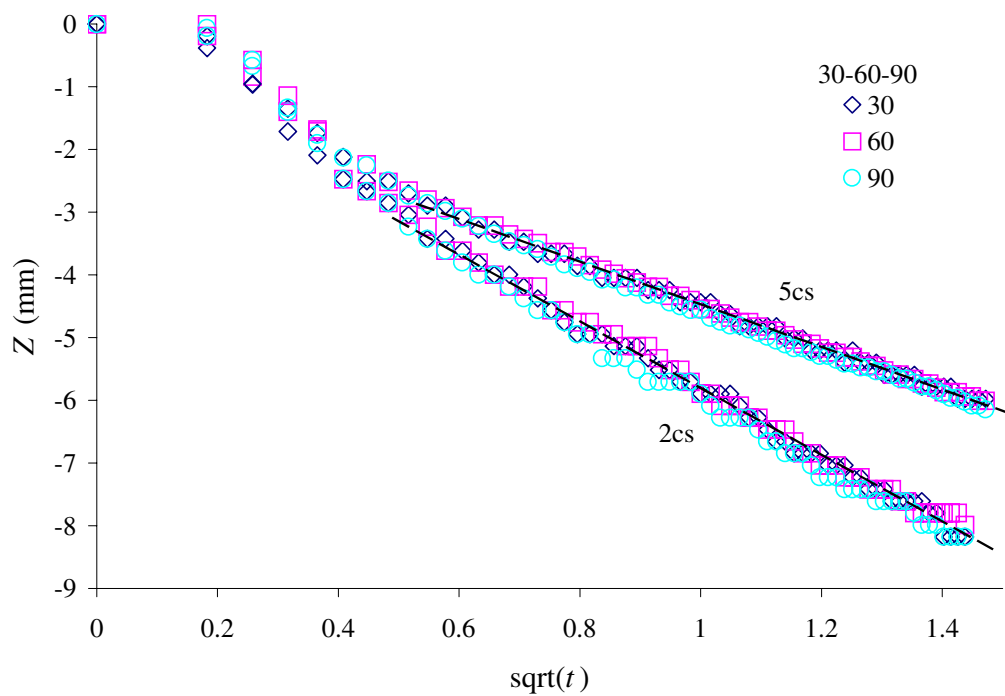

Figure 13. $L(t)$ vs. $t^{1/2}$ for 45-45-90, 5cs.

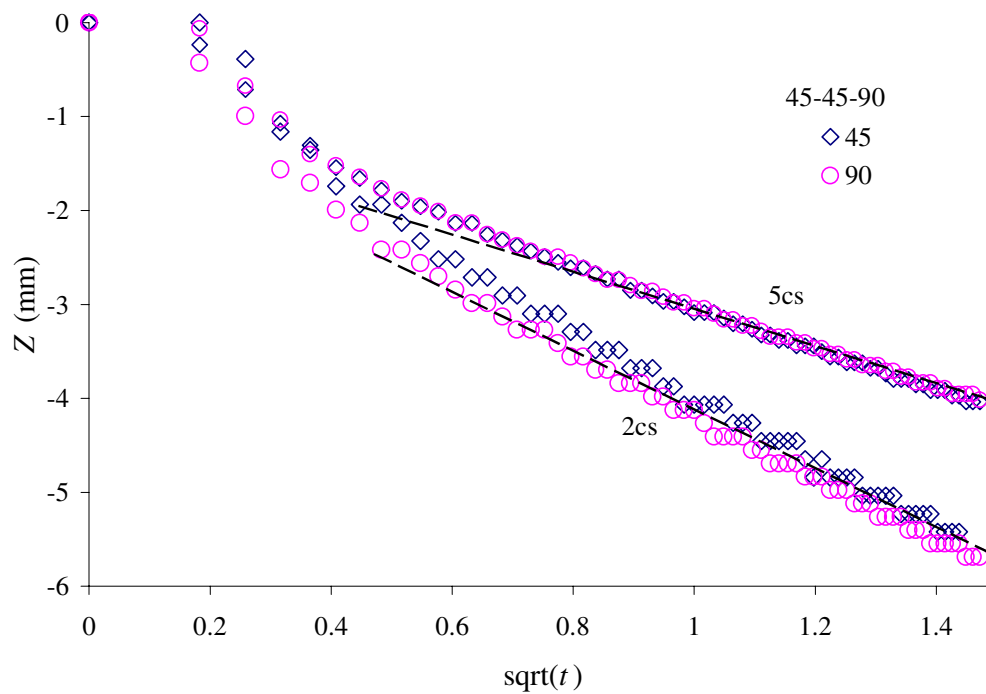Figure 14. $Z(t)$ vs. $t^{1/2}$ for 30-60-90, 2 and 5cs.

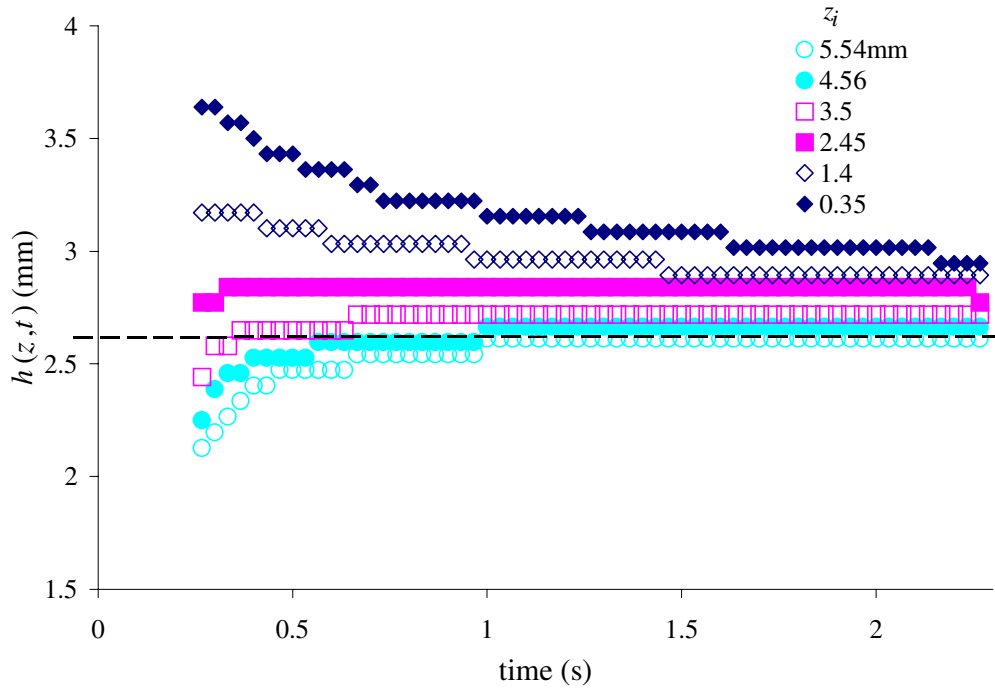Figure 15. $Z(t)$ vs. $t^{1/2}$ for 45-45-90, 2 and 5cs.

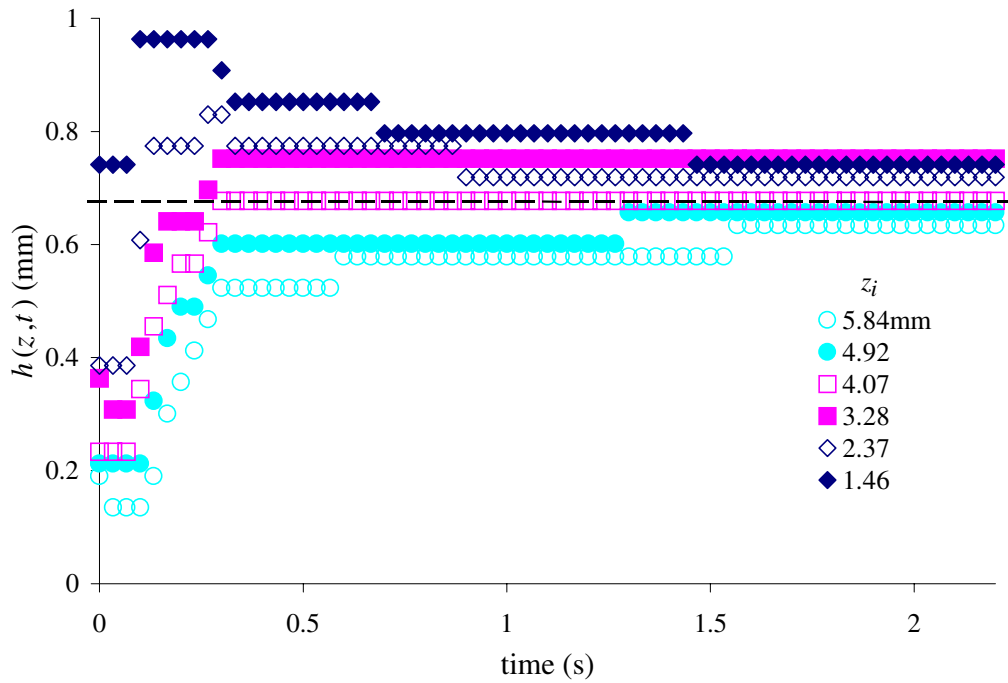Figure 16. $h(z_i,t)$ in 45° corner in 45-45-90, 2cs. Dashed line is theoretical H_{45}=2.63mm, Eq. (13).

Figure 17. $h(z_i,t)$ in 90° corner in 45-45-90, 2cs. Dashed line is theoretical H_{90}=0.67mm, Eq. (13).

Table 1. Computed values for $\overline{\eta}_{br}^+$ for $\theta = 0$. Q_{geom} listed for $A_n = 0.5\text{mm}^2$

Container cross-section	Q_{geom}	$\overline{\eta}_{br}^+$	$\overline{\eta}_{br}^+$
		Eq. (25) Eq. (20)	Eq. (21)
Triangle	30-30-120	1.247	-0.03498	-0.03400
Triangle	30-60-90	0.891	-0.02243	-0.02202
Triangle	30-75-75	0.862	-0.02152	-0.02134
Triangle	36.9-53.1-90	0.742	-0.01802	-0.01774
Triangle	45-45-90	0.683	-0.01638	-0.01614
Triangle	60-60-60	0.470	-0.01068	-0.01056
Eq. Triangle		0.470	-0.01068	-0.01056
Square		0.134	-0.002741	-0.002721
reg-pentagon		0.0537	-0.001052	-0.001045
reg-hexagon		0.0256	-0.000493	-0.000489
reg-octagon		0.00805	-0.000153	-0.000152
Eq. Rhombus	90-90	0.134	-0.002741	-0.002721
Eq. Rhombus	60-120	0.346	-0.007495	-0.007423
Eq. Rhombus	45-135	0.671	-0.01592	-0.01569
Eq. Rhombus	30-150	1.249	-0.03495	-0.03399
Eq. Rhombus	15-165	2.266	-0.09413	-0.08512
Eq. Rhombus	6.5-173.5	3.077	-0.3642 -0.1819	
Eq. Rhombus	0.1-179.9	2.26	--	--
Square		0.134	-0.002740	-0.002721
2:1 Rectangle		0.114	-0.002380	-0.002366
4:1 Rectangle		0.0727	-0.001635	-0.001623

Table 2. Nominal test containers and fluid properties. D_i's are face widths.

Cross-Section	D_1 mm	D_2 mm	D_3 mm	Height mm
30-60-90	9.8	17.0	19.6	150
45-45-90	9.8	9.8	13.6	150

Test Fluid/ Vessel matl.	μ kg/m s	σ N/m	θ deg.	N_D -
2cs Si oil	0.00174	0.0187	0	1.390
5cs Si oil	0.00465	0.0197	0	1.396
Acrylic				1.491

Table 3. Measured and predicted bulk meniscus recede rates for 30-60-90 and 45-45-90 vessels (mm $s^{1/2}$).

Vessel	Fluid	K_Z exp.	K_Z Eq. (22)
30-60-90	2cs	-5.47	-5.67
	5cs	-3.76	-3.60
45-45-90	2cs	-3.3	-3.69
	5cs	-2.1	-2.34

Table 4. Measured and predicted liquid column rise rates for given corner.

Vessel/Fluid	Corner angle	K_L exp.	K_{Lj} theo.
30-60-90/2cs	30	75.3	73.3
	60	50.8	49.4
	90	28.6	28.9
30-60-90/5cs	30	46.4	46.5
	60	50.8	49.4
	90	28.6	28.9
45-45-90/2cs	45	47.2	49.2
	90	21.5	23.2
45-45-90/5cs	45	31.6	31.2
	90	14.0	14.8

REPORT DOCUMENTATION PAGE

1. AGENCY USE ONLY (Leave blank)	2. REPORT DATE	3. REPORT TYPE AND DATES COVERED
	July 2001	Final Contractor Report

4. TITLE AND SUBTITLE

Capillary Flow in Containers of Polygonal Section: Theory and Experiment

5. FUNDING NUMBERS

WU–101–13–0B–00
NAS3–00126

6. AUTHOR(S)

Mark M. Weislogel

7. PERFORMING ORGANIZATION NAME(S) AND ADDRESS(ES)

TDA Research Inc.
12345 W. 52nd Avenue
Wheat Ridge, Colorado 80033–1917

8. PERFORMING ORGANIZATION REPORT NUMBER

E–12777

9. SPONSORING/MONITORING AGENCY NAME(S) AND ADDRESS(ES)

National Aeronautics and Space Administration
Washington, DC 20546–0001

10. SPONSORING/MONITORING AGENCY REPORT NUMBER

NASA CR—2001-210900

11. SUPPLEMENTARY NOTES

Project Manager, Enrique Ramé, Microgravity Science Division, NASA Glenn Research Center, organization code 6712, 216–433–2842.

12a. DISTRIBUTION/AVAILABILITY STATEMENT

Unclassified - Unlimited
Subject Categories: 02, 20, 18, 34, and 44   Distribution: Nonstandard

Available electronically at http://gltrs.grc.nasa.gov/GLTRS

This publication is available from the NASA Center for AeroSpace Information, 301–621–0390.

12b. DISTRIBUTION CODE

13. ABSTRACT (Maximum 200 words)

An improved understanding of the large-length-scale capillary flows arising in a low-gravity environment is critical to that engineering community concerned with the design and analysis of spacecraft fluids management systems. Because a significant portion of liquid behavior in spacecraft is capillary dominated it is natural to consider designs that best exploit the spontaneous character of such flows. In the present work, a recently verified asymptotic analysis is extended to approximate spontaneous capillary flows in a large class of cylindrical containers of irregular polygonal section experiencing a step reduction in gravitational acceleration. Drop tower tests are conducted using partially-filled irregular triangular containers for comparison with the theoretical predictions. The degree to which the experimental data agree with the theory is a testament to the robustness of the basic analytical assumption of predominantly parallel flow. As a result, the closed form analytical expressions presented serve as simple, accurate tools for predicting bulk flow characteristics essential to practical low-g system design and analysis. Equations for predicting corner wetting rates, total container flow rates, and transient surfaces shapes are provided that are relevant also to terrestrial applications such as capillary flow in porous media.

14. SUBJECT TERMS

Capillary flow; Surface tension; Drop tower; Tankage

15. NUMBER OF PAGES
29

16. PRICE CODE

17. SECURITY CLASSIFICATION OF REPORT	18. SECURITY CLASSIFICATION OF THIS PAGE	19. SECURITY CLASSIFICATION OF ABSTRACT	20. LIMITATION OF ABSTRACT
Unclassified	Unclassified	Unclassified	